



RESEARCH

Dynamics and energy harvesting from parametrically coupled self-excited electromechanical oscillator

Godwin Sani · Maksymilian Bednarek ·
Krzysztof Witkowski · Jan Awrejcewicz

Received: 6 March 2024 / Accepted: 28 April 2024
© The Author(s) 2024

Abstract The investigated parametrically coupled electromechanical structure is composed of a mechanical Duffing oscillator whose mass sits on a moving belt surface. The driving electrical network is a van der Pol oscillator whose aim is to actuate the attached DC motor to provide some rotatory unbalances and parametric coupling in the vibrating structure. The coupled oscillator is applied to energy harvesting and overcomes the limitation of low energy generation associated with a single oscillator of this kind. The system was solved analytically and validated by numerical methods. The global dynamics of the structure were investigated, and nonlinear phenomena such as Neimark–Sacker bifurcation, discontinuity-induced bifurcation, grazing–sliding, and bifurcation to multiple tori were identified. These nonlinear behaviors affect the harvested energy at bifurcation points, resulting in jumps from one energy level to another. In addition to harnessing the highest energy under hard parametric coupling, the coupling ensures that higher and more useful energy is harvested over a wider range of belt speeds. Finally, the qualitative validation of the numerical concept by experimental setup verifies the workings of the model.

Keywords Electromechanical · Parametric excitation · Coupled oscillators · Discontinuity-induced bifurcation · Energy harvesting

1 Introduction

Electromechanical oscillations have been found in modern systems such as speakers, specialized sensors, and power grids [1–3]. In power systems, such oscillations pose severe threats to the stable workings of interconnected grids and angular instability [3, 4]. The oscillations stem from associated nonlinearities of power converters and are undesirable, requiring dynamical analysis, damping measurements, and control. Kenmogne et al. [5], however, converted such unwanted oscillations of an electromechanical system with irrational nonlinearities to a novel sand sieve application by analyzing the damping effects on the system’s dynamics. The system consists of an electrically forced van der Pol oscillator magnetically coupled to a network of elastically coupled mechanical subsystems. Other coupled electromechanical systems are the unforced van der Pol and Duffing oscillators with elastic couplings [6], dissipative couplings [7], forced and combined couplings [8], parametric couplings [9]; and have found applications in neuron models, information coding, sensors and actuators such as the skin impedance measurement unit [10]. Despite the notable presence of these coupled oscillators and their dynamical analyses, the configuration with friction-induced excitation

G. Sani · M. Bednarek · K. Witkowski · J. Awrejcewicz (✉)
Department of Automation, Biomechanics and
Mechatronics, Łódź University of Technology,
Stefanowskiego Str. 1/15, 90-924 Lodz, Poland
e-mail: jan.awrejcewicz@p.lodz.pl

is lacking in the literature. Balaram et al. [11] investigated friction-induced stick-slip vibrations in a three degree of freedom (3 DoF) discontinuous model of a disc brake system with the aim of suppressing the unwanted vibration. The undesired oscillations were suppressed using normal harmonic forcing for frequency entrainment of the nonsmooth limit cycles. Similar structures with friction-induced vibration have been carried out by researchers in [12–15], in which a mass on the moving belt forms the central substructure, and the speed of the belt creates the induced self-excitation. Insights into the instability of multi-degree of freedom of such models were investigated by Li et al. [16]. Other structures with friction-induced mechanisms, including constraints and discontinuities are studied in the works [17–21]. Though the dynamics of the highlighted systems were highly investigated, their applications towards energy harvesting were not extended.

Vibration energy harvesting (VEH) utilizing nonlinear and nonideal sources has proven to be vital technology in meeting ever-increasing energy demands [22, 23]. Besides being environmentally friendly, it supplies small electronic devices such as wireless sensor networks, communications device packs, Internet of Things (IoT), wearable medical applications, and transportation systems [24–26]. Wang et al. [27] numerically investigate the conversion of friction-induced vibration (FIV) of mechanical structures composed of mass on a moving belt under normal loads into harvested energy. The study showed that both the normal load and the belt's speed significantly influence generated power, and the energy is greater in the unstable region. A similar investigation was carried out by Han and Zhang [28] for a disc brake system, modeled as a V-shape structure of springs-connected mass on a moving belt. The self-excited system had additional surface nonlinearity of quasi-zero stiffness. The study showed multiple stability of single, double, and triple potential wells and stick-slip motion. An electromagnetic harvester was used to convert the FIV into electrical energy. In another development, Xiang et al. [29] performed a study on a simultaneous FIV reduction and energy harvesting from the braking system of a high-speed train. The harvester serves as a damper for reducing vibrations and, at the same time, converting the FIV into energy. The dynamic contact surface behavior, modeled as an exponential function of the relative speed between the mass and the belt, significantly influenced

the harvested energy. Xiao et al. [30] expanded on similar effects of Stribeck friction surface behaviors (model parameters) of a designed energy generator from FIV in a 1 DoF friction system. The results show that the coefficient of static and dynamic friction, and the exponential decay constant notably affect the energy generation. The FIV systems considered so far are those of rigid mass on belt structures. Chen et al. [31] considered a mass frame that encloses a cantilever with a tip magnet, and a fixed magnet separated by an air gap. The frame rests on the moving belt and converts the FIV into helpful electricity. The stick-slip system is bistable, with poor output power generation in the chaotic region. A more recent study by Sani et al. [32] used a body frame (mass) on the belt, which houses a rotary unbalanced mass that provides parametric excitation as an additional nonideal energy source. The frame was placed on the moving belt so that both the self-excitation from the FIV and the parametric excitation were present. It was demonstrated that while useful energy was harvested due to the surface-excitation alone, the parametric excitation helped to increase the speed bandwidth over which the energy was harvested. The considered literature, in some cases, pointed out the limitation of 1 DoF system, characterized by low energy generation. Where friction-induced vibration of the mass-belt relation was used, energy harvesting was also limited to a small range of belt speeds.

The goal of this study is to overcome these limitations by introducing an electrical subcircuit of the van der Pol oscillator and parametrically coupling it with the mechanical substructure. The advantages are

- (i) The mass on the belt structure allows for the attachment of MFC (piezoelectric) filaments, which are reliable and practical for energy harvesting applications.
- (ii) The parametric coupling of van der Pol subcircuit provides two non-ideal energy sources: the parametric excitation (from the coupling) and the self-excitation from negative damping, of which both inject energy into the system for self-sustained oscillations.
- (iii) Simple enough for energy harvesting applications since only the mechanical subsystem requires physical construction, thus saving costs.

The proposed design overcomes the limitation of low energy harvesting associated with the FIV of 1 DoF substructures and inherent energy harvesting that is

only possible over a small range of belt speeds. The system was solved analytically by multiple scales method, and validated by numerical comparisons of the results. Further contributions include the numerical treatment of the system, which identified the underlying nonlinear dynamic behaviors and their effects on harvested energy. At bifurcation points, there are jumps in the values of harvested energy, while maximum power was generated in the region of hard parametric coupling. Finally, experimental verification of the established model was carried out to validate some known numerical results qualitatively. The rest of the paper is organized as follows. Section 2 deals with system modeling, the governing equations, and the state-space by Filippov method. In section 3, the analytical solution by multiple scale method of the non-resonant scenario, identifying the various resonance conditions in the system, was established. Numerical treatment of the system for bifurcation analysis and effects of the behavioral dynamics on energy were carried out in Sect. 4, while experimental work was performed in Sect. 5. Finally, the concluding remark was given in Sect. 6.

2 System modeling

The conceptual model of the electromechanical system is given in Fig. 1. Let the initial voltage V_c of the capacitor with capacitance C be substantially greater than zero. The current I will flow through the nonlinear resistor R , and the inductor (of inductance, L) feeds the coupling network of drivers $M(t)$ to the stepper motor, which in turn provides some unbalanced rotations on the body mass.

The lumped mass M_0 of the frame with the attached stepper motor is displaced by q . At the same time, the nonlinear stiffness $k(q) = k_1 + k_2q^2$, and the viscous damper d create the restoring forces and cause the mechanical subsystem to act back on the electrical subcircuit via the parametric coupling. Additionally, the mass M_0 is connected with a macro-fiber composite (MFC) piezoelectric crystal for energy harvesting applications. The MFC subcircuit is indicated as having the resistance, capacitance, and equivalent electromechanical coupling coefficient denoted as R_p , C_p , and χ , respectively. When the belt moves at constant speed v_0 , dry frictional force f_r exists between the belt and the mass M_0 and serves as a source of self-excitation to the mechanical subsystem.

It is interesting to show a simple cross-section of the stepper motor and its subcircuit in Fig. 2 where the rotor speed is a function of the number of pole pairs p and rotation angle θ . The direction and speed also depend on the excitation phase and frequency. From the subcircuit of Fig. 2b, R_a and $L_a(\theta)$, represent the resistance and the inductance of phase A winding, respectively. However, the inductance is also a function of the rotor position such that

$$L_a(\theta) = L_0 + L_1 \cos(N_r \theta), \tag{1}$$

where L_0 is the average inductance, L_1 is the maximum inductance variation, and N_r is the rotor teeth number. But if the magnets introduced non-negligible amount of air gap, the winding inductance of the stepper motor is considered to be independent of the rotor position. Then, the back electromotive force (EMF), given by $e_a(\theta)$ becomes a function of the rotor position

$$e_a(\theta) = -p\psi_m \sin(p\theta)\omega, \tag{2}$$

where ψ_m is the motor maximum magnetic flux, and $\omega = \dot{\theta}$. It implies that $\omega \Delta t = \Delta \theta$ for small changes Δ in θ per unit time t , at which point, two pole pairs are energized ($p = 2$). Thus, the parametric coupling $M(t)$ is modeled as

$$M(t) = k_l + k_n \cos(2\omega t), \tag{3}$$

where k_l and k_n are the mutual coupling coefficients due to the interactions between the winding inductances and the magnetic flux of the back EMF. The electromagnetic torque T_e generated [33] is given as

$$T_e = J \frac{d\omega}{dt} + B\omega + T_L, \tag{4}$$

where J is the total inertia, B is the total friction coefficient, and T_L is the load torque. Hence, the system's governing equations can now be established.

2.1 The governing equations

Considering the model in Fig. 1, let Q be the unit charge on the inductive element. The current $I = \frac{dQ}{dt}$ flows in the electrical subcircuit when energized by the capacitive voltage V_c . The nonlinear resistor R offers a dissipative characteristic force that must be normalized. Thus, Q_0 and R_0 are the normalization charge and resistance such that the normalization current is $I_0 = \frac{dQ_0}{dt}$. In our previous studies [9], the governing equations without the moving belt were established using the Euler–Lagrange technique for a system with

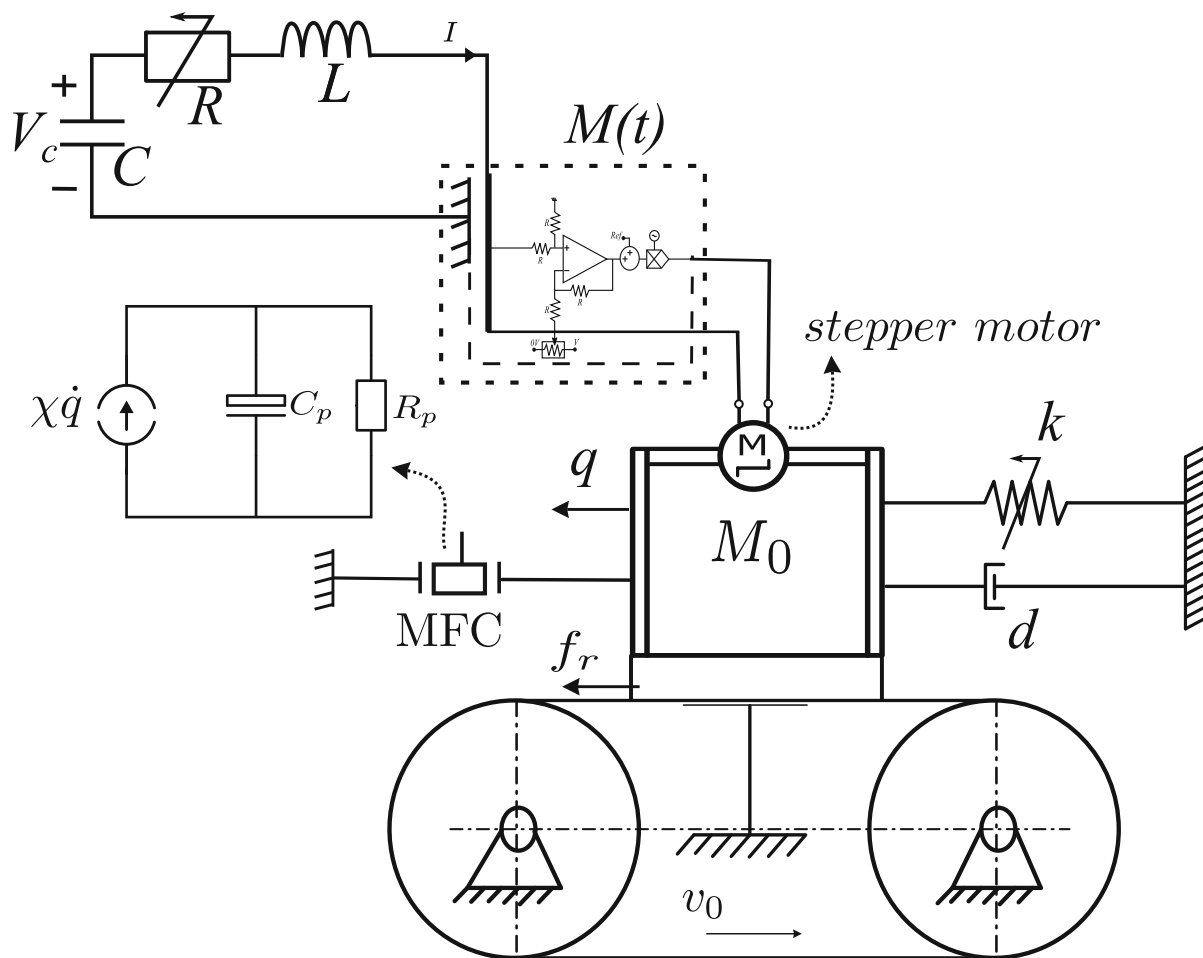


Fig. 1 Conceptual model of the electromechanical system

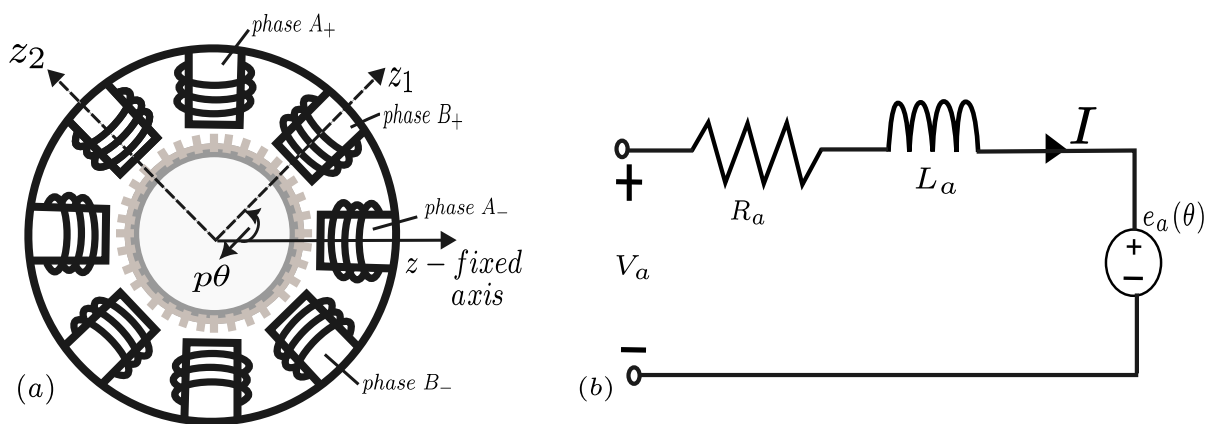


Fig. 2 Stepper Motor cross-section (a) and subcircuit (b)

similar coupling terms. Adopting this approach and including the moving belt mechanism and energy harvesting components, the following governing equations are arrived at:

$$\begin{cases} L \frac{d^2 I}{dt^2} - R_0 \left[1 - \left(\frac{I}{I_0} \right)^2 \right] \frac{dI}{dt} + \frac{I}{C} \\ \quad - (k_l + k_n \cos(2\omega t))(q - I) = 0, \\ M_0 \frac{d^2 q}{dt^2} + d \frac{dq}{dt} + k_1 q + k_2 q^3 + \chi \vartheta - f_r \\ \quad - (k_l + k_n \cos(2\omega t))(I - q) = 0, \\ C_p \frac{d\vartheta}{dt} + \frac{\vartheta}{R_p} - \chi \frac{dq}{dt} = 0, \end{cases} \quad (5)$$

where ϑ is the generated voltage from the MFC piezoelectric crystal of mass m_p , $f_r = M_0 g \mu(v_r)$, and g is the acceleration due to gravity. The relative velocity is $v_r = v_0 - \dot{q}$ and the dry friction coefficient $\mu(v_r)$ is defined as,

$$\begin{cases} \mu(v_r) = \mu_s \operatorname{sgn}(v_r) - \mu_1 v_r + \mu_3 v_r^3, \quad \forall v_0 \neq \dot{q}, \\ \mu(v_r) = 0, \quad \forall v_0 = \dot{q} \end{cases} \quad (6)$$

where the over-dot ($\dot{\cdot}$) represents a time derivative $\frac{d}{dt}$; μ_s , μ_1 , and μ_3 are the coefficients of Stribeck friction model. The first part of Eq. (5) represents the equation of the van der Pol electrical subcircuit, while the second part is that of a mechanical Duffing oscillator on friction-induced surface. The nondimensional form of the system (5)–(6) can now be presented.

2.2 Dimensionless form of the governing equations

Assuming that the natural frequency of the mechanical substructure occurs at the pulsation of the electrical subcircuit,

$$\Omega_e = \frac{1}{\sqrt{LC}} = \sqrt{\frac{k_1}{M_0}}. \quad (7)$$

It follows that Eq. (7) presents the synchronized frequency of the coupled system. Then, the static deflection of the structure is anchored to the normalization current, I_0 such that,

$$y_{st} = \frac{M_0 g}{k_1} \Big|_{I_0 = \dot{Q}_0} \quad (8)$$

Using the dimensionless variables $\tau = \Omega_e t$, $x = \frac{I}{I_0}$, $y = \frac{q}{y_{st}}$, the initial voltage of the MFC crystal is $\vartheta_0 = \frac{m_p g}{\Omega_e R_p C_p}$ so that $\phi = \frac{\vartheta}{\vartheta_0}$. Then, $\frac{d}{dt} = \Omega_e \frac{d}{d\tau}$, $\frac{d^2}{dt^2} =$

$\Omega_e^2 \frac{d^2}{d\tau^2}$, Eqs. (5) and (6) become

$$\begin{cases} \ddot{x} - \alpha (1 - x^2) \dot{x} + x - \lambda N_1 (1 + \mu_p \cos(2\Omega\tau)) \\ \quad \times (y - x) = 0, \\ \ddot{y} + \beta \dot{y} + y + \gamma y^3 + \chi \phi - \rho \mu(\bar{v}_r) \\ \quad - \lambda (1 + \mu_p \cos(2\Omega\tau)) (x - y) = 0, \\ \dot{\phi} + \Theta \phi - \chi \Lambda \dot{y} = 0, \end{cases} \quad (9)$$

and

$$\begin{cases} \mu(\bar{v}_r) = \mu_s \operatorname{sgn}(\bar{v}_r) \\ \quad - \bar{\mu}_1 \bar{v}_r + \bar{\mu}_3 \bar{v}_r^3, \quad \forall v_b \neq \dot{y}, \\ \mu(\bar{v}_r) = 0, \quad \forall v_b = \dot{y}, \end{cases} \quad (10)$$

where $\bar{v}_r = v_b - \dot{y}$, $\alpha = R_0 C \Omega_e$, $\beta = d \sqrt{\frac{1}{k_1 M_0}}$, $\gamma = \frac{k_2 y_{st}^2}{k_1}$, $\Omega = \frac{\omega}{\Omega_e}$, $\lambda = \frac{k_l}{k_1}$, $\mu_p = \frac{k_n}{k_l}$, $\rho = \frac{g}{\Omega_e^2 y_{st}}$, $\Theta = \frac{1}{\Omega_e R_p C_p}$, $\Lambda = \frac{Q_0}{C_p \vartheta_0}$ and $N_1 = C \cdot k_1$, $v_b = \frac{v_0}{\Omega_e y_{st}}$, $\bar{\mu}_1 = \mu_1 \Omega_e y_{st}$, $\bar{\mu}_3 = \mu_3 (\Omega_e y_{st})^3$. It should be noted that Λ and N_1 are dimensionless with $N_1 \leq 1$ because the static deflection y_{st} represents the static charge Q_0 while k_1 transforms into elastance ($\frac{1}{C}$) in electromechanical equivalence.

2.3 State space subdivision by Filippov method

The frictional term $\mu(\bar{v}_r)$ in Eq. (9) makes the vector field associated with the governing system of Eq. (9) discontinuous. Suppose the state space vector is defined as $\{\mathbf{y}\} = \{x, \dot{x}, y, \dot{y}, \phi\}^T$, the surface of discontinuity Σ in the present case can be specified by the scalar function $\Sigma : D(\mathbf{y}) = v_b - \dot{y}$. Using this surface of discontinuity, the five-dimensional state space can be partitioned into three regions:

$$\begin{aligned} S_1 &= \left\{ \mathbf{y} \in \mathfrak{R}^5 : D(\mathbf{y}) < 0 \right\} \\ S_2 &= \left\{ \mathbf{y} \in \mathfrak{R}^5 : D(\mathbf{y}) > 0 \right\} \\ \Sigma &= \left\{ \mathbf{y} \in \mathfrak{R}^5 : D(\mathbf{y}) = 0 \right\} \end{aligned}$$

A pictorial representation of this partitioning is given in Fig. 3. As $\operatorname{sgn}(v_b - \dot{y}) = -1$ when $\mathbf{y} \in S_1$, and $\operatorname{sgn}(v_b - \dot{y}) = +1$ when $\mathbf{y} \in S_2$, the vector field is smooth in regions S_1 and S_2 . These smooth vector fields are denoted as F_1 and F_2 , respectively.

According to the Filippov methodology for discontinuous systems [34], the vector field along the discontinuous surface Σ is defined as a convex combination of the two smooth vector fields.

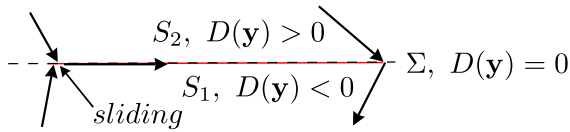


Fig. 3 Surface of discontinuity Σ and the Filippov partitioning

$$\begin{aligned} & \bar{c}_0(F_1(\mathbf{y}), F_2(\mathbf{y})) \\ &= \{F_D : \mathbf{y} \in \mathbb{N}^5 \rightarrow \mathbb{N}^5 : F_D\} \\ &= (1 - \alpha_p)F_1 + \alpha_p F_2, \alpha_p \in [0, 1] \end{aligned} \tag{11}$$

When an orbit, starting out in one region of the state space, intersects with the surface of discontinuity Σ , it can either slide along the surface or transversally cross over to the other region. For illustration, a sliding orbit is shown in Fig. 3. This scheme allows one to formulate the analytical treatment of the discontinuous problem.

3 Analytical solution

The Filippov rendition enables us to solve the system in regions S_1 and S_2 separately by taking $\text{sgn}(v_b - \dot{y}) = -1, +1$ in Eq. (9). This way, we can identify the various resonant conditions present in the system. The solution in the region Σ , however, yields no such information since $\dot{y} = v_b$. It implies that the mass sticks to the belt until slipping occurs, and the convex combination in Eq. (11) applies. Hence, the approximate analytical solution is found only at $\text{sgn}(v_b - \dot{y}) = +1$ for simplicity and further analysis. This solution is valid for all cases since only the sign of μ_s (i.e., $\pm\mu_s$) can be changed without affecting the method. First, Eq. (9) is re-arranged as follows, introducing unit constants to separate the complex terms. We have

$$\begin{cases} \ddot{x} + p_1^2 x - \lambda N_1 y - \alpha(1 - \eta x^2) \dot{x} \\ \quad + \lambda \mu_p N_1 x \cos(2\Omega\tau) - \lambda \mu_p N_1 y \cos(2\Omega\tau) = 0 \\ \ddot{y} + p_2^2 y - \lambda x + \beta \dot{y} + \gamma y^3 + \chi \phi \\ \quad - \rho(\bar{\mu}_s + \bar{\mu}_3(v_b - \kappa \dot{y})^3 - \bar{\mu}_1(v_b - \dot{y})) \\ \quad - \lambda \mu_p x \cos(2\Omega\tau) + \lambda \mu_p y \cos(2\Omega\tau) = 0, \\ \dot{\phi} + \Theta \phi - \chi \Lambda \dot{y} = 0, \end{cases} \tag{12}$$

where $p_1^2 = (1 + \lambda N_1)$, $p_2^2 = (1 + \lambda)$, $\eta = \kappa = 1$. The initial conditions are

$$\begin{aligned} x(0) &= x_0, \dot{x}(0) = v_{x0}, y(0) = y_0, \dot{y}(0) = v_{y0}, \\ \phi(0) &= \phi_0. \end{aligned} \tag{13}$$

The analytical solution is sought using the multiple scales method in the time domain (MSM). Awrejcewicz et al. [35] established the computational sequence of this method herein adopted. We introduce a book-keeping parameter ε , and use two-time scales on the dimensionless time τ . The time-scales τ_0, τ_1 are related as

$$\tau_r = \varepsilon^r \tau, \quad r = 0, 1. \tag{14}$$

Then, the solutions and auxiliary functions are approximated by the following asymptotic expansions

$$\begin{cases} x(\tau; \varepsilon) = \sum_{k=1}^2 \varepsilon^k \xi_k(\tau_0, \tau_1) + O(\varepsilon^3) \\ y(\tau; \varepsilon) = \sum_{k=1}^2 \varepsilon^k \varphi_k(\tau_0, \tau_1) + O(\varepsilon^3) \\ \phi(\tau; \varepsilon) = \sum_{k=1}^2 \varepsilon^k \Phi_k(\tau_0, \tau_1) + O(\varepsilon^3), \end{cases} \tag{15}$$

where the function $\xi_k(\tau_0, \tau_1)$, $\varphi_k(\tau_0, \tau_1)$ and $\Phi_k(\tau_0, \tau_1)$ are to be found. Those of order $O(\varepsilon^3)$ and above are neglected. The differential operators relating to the non-dimensional time τ , and assumptions on the system's parameters for non-resonant solutions are as follows.

$$\begin{aligned} \frac{d}{d\tau} &= D_0 + \varepsilon D_1 + \dots, \quad \frac{d^2}{d\tau^2} \\ &= D_0^2 + 2\varepsilon D_0 D_1 + \varepsilon^2 D_1^2 + \dots, \quad D_r^j = \frac{\partial^j}{\partial \tau_r^j} \end{aligned} \tag{16}$$

$$\begin{cases} \alpha = \varepsilon \tilde{\alpha}, \quad \beta = \varepsilon \tilde{\beta}, \quad \lambda = \varepsilon \tilde{\lambda}, \quad \eta = \varepsilon^{-2} \tilde{\eta}, \\ \kappa = \varepsilon^{-1} \tilde{\kappa}, \quad \gamma = \varepsilon^{-1} \tilde{\gamma}, \\ \Lambda = \varepsilon^{-1} \tilde{\Lambda}, \quad \chi = \varepsilon \tilde{\chi}, \quad \rho = \varepsilon^2 \tilde{\rho}, \end{cases} \tag{17}$$

where $\tilde{\alpha}, \tilde{\beta}, \tilde{\lambda}, \tilde{\eta}, \tilde{\kappa}, \tilde{\gamma}, \tilde{\Lambda}, \tilde{\chi}$ and $\tilde{\rho}$ are of the order 1.

3.1 Non-resonant solution

Substituting the relations (17) into the modified Eqs. (12), and considering the asymptotic expansions (15), the time scaling (14) and the time derivatives (16), the following expressions are yielded according to the ordered powers of ε .

For order "1":

$$D_0^2 \xi_1 + p_1^2 \xi_1 = 0 \tag{18}$$

$$D_0^2 \varphi_1 + p_2^2 \varphi_1 = 0 \tag{19}$$

$$D_0 \Phi_1 + \Theta \Phi_1 - \tilde{\Lambda} \tilde{\chi} D_0 \varphi_1 = 0 \tag{20}$$

For order "2":

$$\begin{aligned}
 D_0^2 \xi_2 + p_1^2 \xi_2 &= -\xi_1 N_1 \tilde{\lambda} \mu_p \cos(2\Omega\tau_0) \\
 &+ N_1 \varphi_1 \tilde{\lambda} \mu_p \cos(2\Omega\tau_0) - \\
 D_0 \xi_1^3 \tilde{\alpha} \tilde{\eta} + D_0 \xi_1 \tilde{\alpha} & \\
 &+ N_1 \varphi_1 \tilde{\lambda} - 2D_0 D_1 \xi_1 \quad (21)
 \end{aligned}$$

$$\begin{aligned}
 D_0^2 \varphi_2 + p_2^2 \varphi_2 &= \\
 -3D_0 \varphi_1 \tilde{\mu}_3 \tilde{\kappa} \tilde{\rho} v_b^2 & \\
 + 3D_0^2 \varphi_1^2 \tilde{\mu}_3 \tilde{\kappa}^2 \tilde{\rho} v_b + \tilde{\mu}_3 \tilde{\rho} v_b^3 - \tilde{\mu}_1 \tilde{\rho} v_b - & \\
 D_0^3 \varphi_1^3 \tilde{\mu}_3 \tilde{\kappa}^3 \tilde{\rho} + \tilde{\rho} \tilde{\mu}_s + \xi_1 \tilde{\lambda} \mu_p \cos(2\Omega\tau_0) & \\
 - \varphi_1 \tilde{\lambda} \mu_p \cos(2\Omega\tau_0) - \varphi_1^3 \tilde{\gamma} - & \\
 D_0 \varphi_1 \tilde{\beta} + \xi_1 \tilde{\lambda} & \\
 - \Phi_1 \tilde{\chi} - 2D_0 D_1 \varphi_1 & \quad (22)
 \end{aligned}$$

$$\begin{aligned}
 D_0 \Phi_2 + \Theta \Phi_2 - \tilde{\Lambda} \tilde{\chi} D_0 \varphi_2 &= D_1 \varphi_1 \tilde{\Lambda} \tilde{\chi} \\
 + D_0 \varphi_2 \tilde{\Lambda} \tilde{\chi} - D_1 \Phi_1 & \quad (23)
 \end{aligned}$$

The solutions to Eqs. (18)–(20) are

$$\xi_1(\tau_0, \tau_1) = B_1(\tau_1) e^{ip_1\tau_0} + \tilde{B}_1(\tau_1) e^{-ip_1\tau_0} \quad (24)$$

$$\varphi_1(\tau_0, \tau_1) = B_2(\tau_1) e^{ip_2\tau_0} + \tilde{B}_2(\tau_1) e^{-ip_2\tau_0}, \quad (25)$$

$$\begin{aligned}
 \Phi_1(\tau_0, \tau_1) &= \frac{p_2 \tilde{\Lambda} \tilde{\chi} B_2(\tau_1) e^{ip_2\tau_0}}{p_2 - i\Theta} \\
 &+ \frac{p_2 \tilde{\Lambda} \tilde{\chi} \tilde{B}_2(\tau_1) e^{-ip_2\tau_0}}{p_2 + i\Theta}, \quad (26)
 \end{aligned}$$

where $B_j(\tau_1)$ ($j = 1, 2$) are unknown functions of slow time scale, and $\tilde{B}_j(\tau_1)$ are their complex conjugates. Substituting (24)–(26) into (21)–(23) leads to the emergence of secular terms. Eliminating the secular terms provides the following solvability conditions and their conjugate reflectors.

$$\begin{aligned}
 -i B_1^2 p_1 \tilde{\alpha} \tilde{B}_1 \tilde{\eta} & \\
 + i B_1 p_1 \tilde{\alpha} - 2i p_1 D_1 B_1 &= 0 \quad (27)
 \end{aligned}$$

$$\begin{aligned}
 -3i B_2 p_2 \tilde{\mu}_3 \tilde{\kappa} \tilde{\rho} v_b^2 - 3i B_2^2 p_2^3 \tilde{\mu}_3 \tilde{B}_2 \tilde{\kappa}^3 \tilde{\rho} & \\
 -3B_2^2 \tilde{B}_2 \tilde{\gamma} - i B_2 p_2 \tilde{\beta} - & \\
 \frac{B_2 p_2 \tilde{\Lambda} \tilde{\chi}^2}{p_2 - i\Theta} - 2i p_2 D_1 B_2 &= 0 \quad (28)
 \end{aligned}$$

Removing the secular terms after substituting (24)–(26) into (21)–(23), one obtains

$$\begin{aligned}
 \xi_2(\tau_0, \tau_1) & \\
 &= \frac{B_1 N_1 \tilde{\lambda} \mu_p e^{i\tau_0(2\Omega+p_1)}}{8\Omega(\Omega+p_1)} \\
 &+ \frac{B_2 N_1 \tilde{\lambda} \mu_p e^{i\tau_0(2\Omega+p_2)}}{2(-2\Omega+p_1-p_2)(2\Omega+p_1+p_2)} \\
 &+ \frac{N_1 \tilde{B}_1 \tilde{\lambda} \mu_p e^{i\tau_0(2\Omega-p_1)}}{8\Omega(\Omega-p_1)} \\
 &+ \frac{N_1 \tilde{B}_2 \tilde{\lambda} \mu_p e^{i\tau_0(2\Omega-p_2)}}{2(2\Omega+p_1-p_2)(-2\Omega+p_1+p_2)} \\
 &+ \frac{B_2 N_1 \tilde{\lambda} e^{ip_2\tau_0}}{(p_1-p_2)(p_1+p_2)} \\
 &+ \frac{i B_1^3 \tilde{\alpha} \tilde{\eta} e^{3ip_1\tau_0}}{8p_1} + CC, \quad (29)
 \end{aligned}$$

$$\begin{aligned}
 \varphi_2(\tau_0, \tau_1) & \\
 &= B_2^2 \tilde{\mu}_3 \tilde{\kappa}^2 \tilde{\rho} v_b e^{2ip_2\tau_0} + 6B_2 \tilde{\mu}_3 \tilde{B}_2 \tilde{\kappa}^2 \tilde{\rho} v_b \\
 &- \frac{\tilde{\mu}_3 \tilde{\rho} v_b^3 + \tilde{\mu}_1 \tilde{\rho} v_b + \tilde{\rho} \tilde{\mu}_s}{p_2^2} \\
 &- \frac{e^{3ip_2\tau_0} (-B_2^3 \tilde{\gamma} + i B_2^3 p_2^3 \tilde{\mu}_3 \tilde{\kappa}^3 \tilde{\rho})}{8p_2^2} \\
 &+ \frac{B_2 \tilde{\lambda} \mu_p e^{i\tau_0(2\Omega+p_2)}}{8\Omega(\Omega+p_2)} \\
 &- \frac{B_1 \tilde{\lambda} \mu_p e^{i\tau_0(2\Omega+p_1)}}{2(2\Omega+p_1-p_2)(2\Omega+p_1+p_2)} \\
 &- \frac{\tilde{B}_1 \tilde{\lambda} \mu_p e^{i\tau_0(2\Omega-p_1)}}{2(2\Omega-p_1-p_2)(2\Omega-p_1+p_2)} \\
 &+ \frac{\tilde{B}_2 \tilde{\lambda} \mu_p e^{i\tau_0(2\Omega-p_2)}}{8\Omega(\Omega-p_2)} \\
 &- \frac{B_1 \tilde{\lambda} e^{ip_1\tau_0}}{(p_1-p_2)(p_1+p_2)} + CC, \quad (30)
 \end{aligned}$$

$$\begin{aligned} \Phi_2(\tau_0, \tau_1) = & \frac{2B_2^2 p_2 \bar{\mu}_3 \tilde{\kappa}^2 \tilde{\Lambda} \tilde{\rho} \tilde{\chi} v_b e^{2ip_2 \tau_0}}{2p_2 - i\Theta} - \frac{ie^{3ip_2 \tau_0} \left(\frac{3}{8} B_2^3 p_2^2 \bar{\mu}_3 \tilde{\kappa}^3 \tilde{\Lambda} \tilde{\rho} \tilde{\chi} + \frac{3iB_2^3 \tilde{\gamma} \tilde{\Lambda} \tilde{\chi}}{8p_2} \right)}{3p_2 - i\Theta} \\ & - \frac{ie^{i\tau_0(2\Omega+p_1)} \left(-\frac{i\Omega B_1 \tilde{\lambda} \tilde{\Lambda} \tilde{\chi} \mu_p}{4\Omega^2+4\Omega p_1+p_1^2-p_2^2} - \frac{iB_1 p_1 \tilde{\lambda} \tilde{\Lambda} \tilde{\chi} \mu_p}{2(4\Omega^2+4\Omega p_1+p_1^2-p_2^2)} \right)}{2\Omega - i\Theta + p_1} \\ & - \frac{ie^{i\tau_0(2\Omega-p_1)} \left(\frac{ip_1 \tilde{B}_1 \tilde{\lambda} \tilde{\Lambda} \tilde{\chi} \mu_p}{2(4\Omega^2-4\Omega p_1+p_1^2-p_2^2)} - \frac{i\Omega \tilde{B}_1 \tilde{\lambda} \tilde{\Lambda} \tilde{\chi} \mu_p}{4\Omega^2-4\Omega p_1+p_1^2-p_2^2} \right)}{2\Omega - i\Theta - p_1} \\ & - \frac{ie^{i\tau_0(2\Omega+p_2)} \left(-\frac{iB_2 p_2^2 \tilde{\lambda} \tilde{\Lambda} \tilde{\chi} \mu_p}{8\Omega(\Omega-p_2)(\Omega+p_2)} - \frac{iB_2 p_2 \tilde{\lambda} \tilde{\Lambda} \tilde{\chi} \mu_p}{8(\Omega-p_2)(\Omega+p_2)} + \frac{i\Omega B_2 \tilde{\lambda} \tilde{\Lambda} \tilde{\chi} \mu_p}{4(\Omega-p_2)(\Omega+p_2)} \right)}{2\Omega - i\Theta + p_2} \\ & - \frac{ie^{i\tau_0(2\Omega-p_2)} \left(\frac{i\tilde{B}_2 \tilde{\lambda} \tilde{\Lambda} \tilde{\chi} \mu_p}{4(\Omega-p_2)} - \frac{ip_2 \tilde{B}_2 \tilde{\lambda} \tilde{\Lambda} \tilde{\chi} \mu_p}{8\Omega(\Omega-p_2)} \right)}{2\Omega - i\Theta - p_2} + \frac{B_1 p_1 \tilde{\lambda} \tilde{\Lambda} \tilde{\chi} e^{ip_1 \tau_0}}{(p_1^2 - p_2^2)(p_1 - i\Theta)} + \text{CC}, \end{aligned} \tag{31}$$

where CC stands for the complex conjugate terms. The complex functions B_j , and \tilde{B}_j are dependent on τ_1 , and are found from the solvability conditions (27)–(28) as follows;

$$\begin{aligned} B_i(\tau_1) &= \frac{1}{2} b_i(\tau_1) e^{i\psi_i(\tau_1)}, \\ \tilde{B}_i(\tau_1) &= \frac{1}{2} b_i(\tau_1) e^{-i\psi_i(\tau_1)}, \quad i = 1, 2 \end{aligned} \tag{32}$$

where $a_i(\tau_1)$ and $\psi_i(\tau_1)$ are real-valued.

Putting (32) in (27)–(28), separating the imaginary and real parts,

$$b'_1 = -\frac{1}{8} b_1 \tilde{\alpha} \left(b_1^2 \tilde{\eta} - 4 \right), \tag{33}$$

$$\psi'_1 = 0, \tag{34}$$

$$\begin{aligned} b'_2 &= \frac{1}{8} b_2 \left(-3\bar{\mu}_3 \tilde{\kappa} \tilde{\rho} \left(b_2^2 p_2^2 \tilde{\kappa}^2 + 4v_b^2 \right) \right. \\ &\quad \left. - 4\tilde{\beta} - \frac{4\Theta \tilde{\Lambda} \tilde{\chi}^2}{\Theta^2 + p_2^2} \right), \end{aligned} \tag{35}$$

$$\psi'_2 = \frac{3b_2^2 \tilde{\gamma}}{8p_2} + \frac{p_2 \tilde{\Lambda} \tilde{\chi}^2}{2(\Theta^2 + p_2^2)}. \tag{36}$$

The reconstitution of Eqs. (33)–(36) into the original time scale τ is carried out using $a_i(\tau) = \varepsilon b_i$, and the reverse assumptions in (17),

$$a'_1 = -\frac{1}{8} a_1 \alpha \left(a_1^2 \eta - 4 \right), \tag{37}$$

$$\psi'_1 = 0, \tag{38}$$

$$\begin{aligned} a'_2 &= \frac{1}{8} a_2 \left(-3\bar{\mu}_3 \kappa \rho \left(a_2^2 p_2^2 \kappa^2 + 4v_b^2 \right) \right. \\ &\quad \left. - 4\beta - \frac{4\Theta \Lambda \chi^2}{\Theta^2 + p_2^2} \right), \end{aligned} \tag{39}$$

$$\psi'_2 = \frac{3a_2^2 \gamma}{8p_2} + \frac{p_2 \Lambda \chi^2}{2(\Theta^2 + p_2^2)}. \tag{40}$$

Eqs. (37)–(40) are the modulation equations in time τ , with initial conditions

$$a_1(0) = a_{10}, \quad a_2(0) = a_{20}, \quad \psi_1(0) = \psi_{10}, \quad \psi_2(0) = \psi_{20}. \tag{41}$$

The quantities a_{10} , a_{20} , ψ_{10} , and ψ_{20} are connected with the initial values x_0 , v_{y0} , y_0 , v_{y0} , and ϕ_0 in (13). However, due to nonlinearity in (37)–(40), the solutions are found using the *NDSolve* function in Mathematica software. Combining all the solutions from (24)–(25), and (29)–(30) in a reconstituted form, the following analytical solutions are obtained.

$$\begin{aligned} x(\tau) &= \frac{a_1 \lambda N_1 \mu_p \cos(\tau(2\Omega - p_1) - \psi_1)}{8\Omega(\Omega - p_1)} \\ &\quad + \frac{a_1 \lambda N_1 \mu_p \cos(\tau(p_1 + 2\Omega) + \psi_1)}{8\Omega(p_1 + \Omega)} \\ &\quad + \frac{a_2 \lambda N_1 \mu_p \cos(\tau(2\Omega - p_2) - \psi_2)}{2(p_1 - p_2 + 2\Omega)(p_1 + p_2 - 2\Omega)} \\ &\quad - \frac{a_2 \lambda N_1 \mu_p \cos(\tau(p_2 + 2\Omega) + \psi_2)}{2(-p_1 + p_2 + 2\Omega)(p_1 + p_2 + 2\Omega)} \end{aligned}$$

$$\begin{aligned}
 &+ \frac{a_2 \lambda N_1 \cos(p_2 \tau + \psi_2)}{(p_1 - p_2)(p_1 + p_2)} \\
 &- \frac{\alpha a_1^3 \eta \sin(3(p_1 \tau + \psi_1))}{32 p_1} \\
 &+ a_1 \cos(p_1 \tau + \psi_1), \tag{42}
 \end{aligned}$$

$$\begin{aligned}
 y(\tau) &= a_2 \cos(p_2 \tau + \psi_2) + \frac{1}{2} a_2^2 \kappa^2 \rho \bar{\mu}_3 v_b \cos(2(p_2 \tau + \psi_2)) \\
 &+ \frac{3}{2} a_2^2 \kappa^2 \rho \bar{\mu}_3 v_b \\
 &+ \frac{a_2^3 (\kappa^3 p_2^3 \rho \bar{\mu}_3 \sin(3(p_2 \tau + \psi_2)) + \gamma \cos(3(p_2 \tau + \psi_2)))}{32 p_2^2} \\
 &- \frac{\rho (\bar{\mu}_3 v_b^3 + \bar{\mu}_1 v_b + \bar{\mu}_s)}{p_2^2} \\
 &+ \frac{a_2 \lambda \mu_p \cos(\tau(2\Omega - p_2) - \psi_2)}{8\Omega(\Omega - p_2)} \\
 &+ \frac{a_2 \lambda \mu_p \cos(\tau(p_2 + 2\Omega) + \psi_2)}{8\Omega(p_2 + \Omega)} \\
 &- \frac{a_1 \lambda \cos(p_1 \tau + \psi_1)}{(p_1 - p_2)(p_1 + p_2)} \\
 &- \frac{a_1 \lambda \mu_p \cos(\tau(2\Omega - p_1) - \psi_1)}{2(-p_1 - p_2 + 2\Omega)(-p_1 + p_2 + 2\Omega)} \\
 &- \frac{a_1 \lambda \mu_p \cos(\tau(p_1 + 2\Omega) + \psi_1)}{2(p_1 - p_2 + 2\Omega)(p_1 + p_2 + 2\Omega)}, \tag{43}
 \end{aligned}$$

where

$$\begin{aligned}
 cn(\tau) &= \cos(3(p_2 \tau + \psi_2)), \\
 sn(\tau) &= \sin(3(p_2 \tau + \psi_2)), \\
 R_1 &= \lambda \Lambda \chi \mu_p (p_1 + 2\Omega), R_2 = \lambda \Lambda \chi \mu_p (2\Omega - p_1), \\
 R_3 &= \lambda \Lambda \chi \mu_p (p_2 + 2\Omega), R_4 = \lambda \Lambda \chi \mu_p (2\Omega - p_2).
 \end{aligned}$$

The time-dependent functions $a_j(\tau)$ and $\psi_j(\tau)$ are the amplitudes and phases of the modulation equations (37)–(40).

Using the following set of fixed parameters: $\eta = 1$, $\kappa = 1$, $\alpha = 0.06$, $\beta = 0.03$, $\gamma = 0.01$, $\lambda = 0.179$, $\mu_p = 0.12$, $N_1 = -0.209$, $p_1 = 1.001$, $p_2 = 1.4$, $\chi = 0.000002$, $\Lambda = 5000000$, $\Theta = 0.000003$, $\rho = 1$, $\Omega = 2.095$, $v_b = 0.06$, $\mu_s = 0.001$, $\bar{\mu}_1 = 0.02232$, $\bar{\mu}_3 = 1.1191$, and the initial values: $a_{10} = -0.04$, $a_{20} = 0.0$, $\psi_{10} = 0.0$, $\psi_{20} = 0.0$, the initial conditions for the numerical simulation were estimated from (42)–(44) as $x_0 = -0.0399867$, $v_{x0} = -0.00119876$, $y_0 = -0.0087211$, $v_{y0} = -0.00022204$, $\phi_0 = -0.074043$. Figures 4 and 5 compare the short-time and long-time histories for x and y , respectively, obtained by the analytical (MSM) with the corresponding numerical solutions. There is a high degree of compliance between the solutions methods. Though other sets of initial values could be used, the choice of the value of a_{10} , which represents the initial displacement of the mass, is crucial for the parametrically coupled oscillators to

$$\begin{aligned}
 \phi(\tau) &= \frac{a_2^2 \kappa^2 \Lambda p_2 \rho \chi \bar{\mu}_3 v_b (2 p_2 \cos(2(p_2 \tau + \psi_2)) - \Theta \sin(2(p_2 \tau + \psi_2)))}{\Theta^2 + 4 p_2^2} \\
 &+ \frac{3 a_2^3 \Lambda \chi (\kappa^3 p_2^3 \rho \bar{\mu}_3 (\Theta cn(\tau) + 3 p_2 sn(\tau)) + \gamma (3 p_2 cn(\tau) - \Theta sn(\tau)))}{32 p_2 (\Theta^2 + 9 p_2^2)} \\
 &+ \frac{a_2 R_3 ((p_2 + 2\Omega) \cos(\tau(p_2 + 2\Omega) + \psi_2) - \Theta \sin(\tau(p_2 + 2\Omega) + \psi_2))}{8\Omega(p_2 + \Omega)(\Theta^2 + 4 p_2 \Omega + p_2^2 + 4\Omega^2)} \\
 &+ \frac{a_2 R_4 ((2\Omega - p_2) \cos(\tau(2\Omega - p_2) - \psi_2) - \Theta \sin(\tau(2\Omega - p_2) - \psi_2))}{8\Omega(\Omega - p_2)(\Theta^2 - 4 p_2 \Omega + p_2^2 + 4\Omega^2)} \\
 &- \frac{a_1 R_2 ((2\Omega - p_1) \cos(\tau(2\Omega - p_1) - \psi_1) - \Theta \sin(\tau(2\Omega - p_1) - \psi_1))}{2(-4 p_1 \Omega + p_1^2 - p_2^2 + 4\Omega^2)(\Theta^2 - 4 p_1 \Omega + p_1^2 + 4\Omega^2)} \\
 &- \frac{a_1 R_1 ((p_1 + 2\Omega) \cos(\tau(p_1 + 2\Omega) + \psi_1) - \Theta \sin(\tau(p_1 + 2\Omega) + \psi_1))}{2(4 p_1 \Omega + p_1^2 - p_2^2 + 4\Omega^2)(\Theta^2 + 4 p_1 \Omega + p_1^2 + 4\Omega^2)} \\
 &+ \frac{a_1 \lambda \Lambda p_1 \chi (\Theta \sin(p_1 \tau + \psi_1) - p_1 \cos(p_1 \tau + \psi_1))}{(p_1^2 - p_2^2)(\Theta^2 + p_1^2)} \\
 &+ \frac{a_2 \Lambda p_2 \chi (p_2 \cos(p_2 \tau + \psi_2) - \Theta \sin(p_2 \tau + \psi_2))}{\Theta^2 + p_2^2}, \tag{44}
 \end{aligned}$$

Fig. 4 Compared time histories of x-coordinate

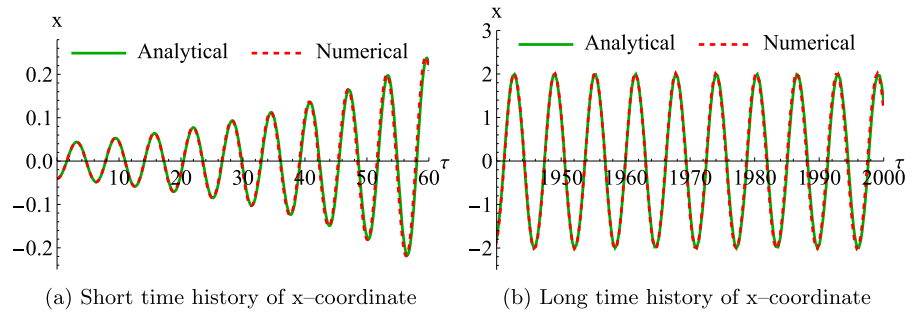


Fig. 5 Compared time histories of y-coordinate

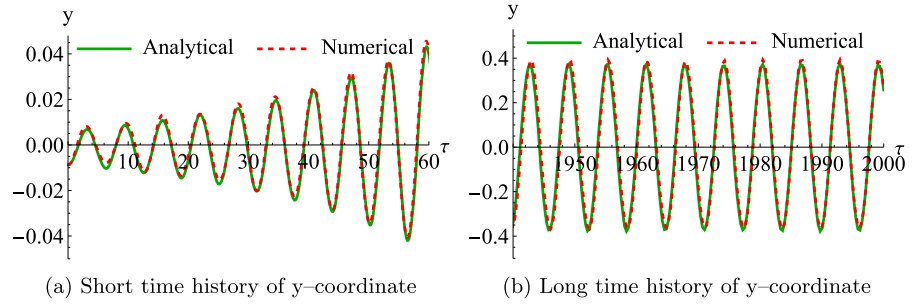
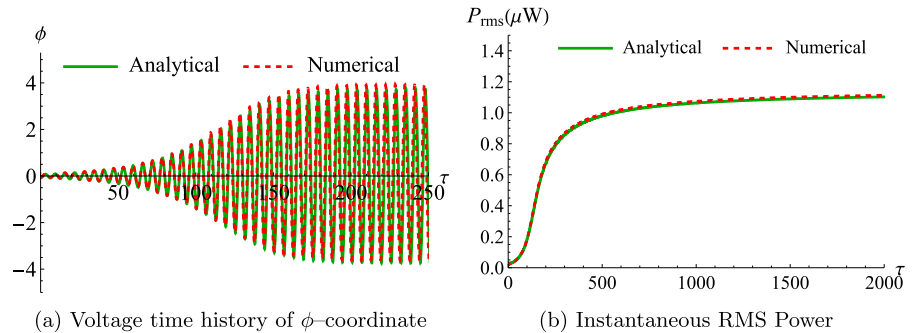


Fig. 6 Compared time histories of voltage (ϕ -coordinate) and the RMS power



have immediate influences on each other. However, this value and those of the system parameters are assumed to be small in order to minimize computational errors.

On the harvested energy, Fig. 6 is added to show the generated dimensionless voltage time-histories (Fig. 6a) and the dimensional instantaneous root mean square (RMS) power (Fig. 6b), computed based on metrics established in Sect. 4. The results are also well-matched between the analytical and numerical solutions. The RMS power increases at the instance of time until the steady state, where it is fairly held constant. Additionally, the following resonances are identified from Eqs. (42)–(44) where the terms with negative operands in the denominators are equated to zero.

- (i) Primary parametric resonances at $\Omega \approx p_1, \Omega \approx p_2$;
- (ii) Combined parametric resonances at $\Omega \approx \frac{1}{2}(-p_1 + p_2), \Omega \approx \frac{1}{2}(p_1 - p_2), \Omega \approx \frac{1}{2}(p_1 + p_2)$;

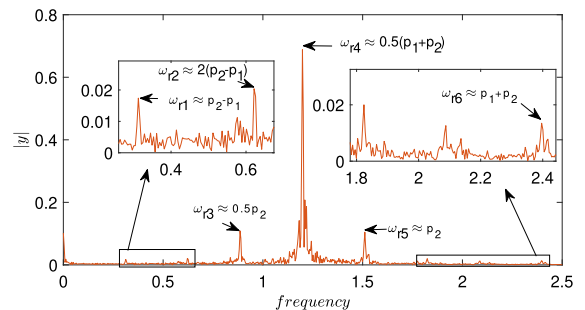


Fig. 7 Frequency response of the system with identified parametric resonances

- (iii) Internal resonance at $p_1 \approx p_2$.

Figure 7 presents the frequency response of the y solution showing some identified primary and combined parametric resonance $w_{rj}, j = 1, 2, \dots, 5$. These resonant points were identified based on the fixed

Table 1 Compliance errors

Error metric	x	y	ϕ
RMSE	5.89491×10^{-5}	7.50036×10^{-6}	7.50033×10^{-6}
MAE	3.50942×10^{-5}	4.63146×10^{-6}	4.63141×10^{-6}

data set used. The greatest (combined) parametric resonance occurs at $w_{r4} \approx \frac{1}{2}(p_1 + p_2)$. It is closely guided by the primary resonance and its harmonic at $w_{r5} = p_2$ and $w_{r3} = \frac{1}{2}p_2$.

The approximate solutions presented here are valid only for the non-resonant case. At resonance, some modifications must be made to accommodate the resonance-causing terms, which are outside the aim of the present study. Furthermore, the computations are based on small identified parameter values to minimize errors. The assumptions in (14)–(17) truncate the asymptotic expansion of the assumed solution. However, they ensure that all the terms in the governing equations are captured in solution procedures. It implies that the compliance errors are only limited to the truncation of asymptotic solutions by two-time scales.

3.2 Compliance error

Compliance error is the difference between the analytical solution and the numerical solution computed based on two well-known metrics: the root mean square error (RMSE) and the mean absolute error (MAE) according to the following equations [36], where RMSE measures the robustness of the method, and MAE indicates the estimation accuracy of the analytical process.

$$\begin{cases} RMSE = \sqrt{\frac{\sum_{j=1}^N E_j^2}{N}}, \\ MAE = \frac{\sum_{j=1}^N |E_j|}{N}, \end{cases} \quad (45)$$

where E is the difference between the numerical and approximate analytical solutions, evaluated at time interval j to N . For ease of calculation, N is fixed at 1010. Table 1 shows the compliance errors of the computations. The errors are of the order of $10^{-5}/10^{-6}$, which portends the solutions’ robustness and accuracy.

4 Numerical treatment

The Filippov rendition of the system in section 2.3 also allows one to obtain a smooth approximation of the surface of discontinuity in state-space by applying Eq. (11). This way, the system’s global dynamics can be investigated via the bifurcation analysis. The effects of these dynamics on harvested energy can also be numerically examined. The non-dimensional RMS voltage is computed by

$$V_{rms} = \sqrt{\frac{1}{n} \sum_j^n \phi_j^2}, \quad j = 1, 2, 3, \dots, n; \quad (46)$$

and n is the approximate period (or its multiple) of the generated non-dimensional voltage ϕ . The dimensional value of RMS voltage is, however, $\tilde{V}_{rms} = \vartheta_0 V_{rms}$. The value of ϑ_0 can be found using the expression given in Sect. 2.2 as $\vartheta_0 = \frac{m_p g}{\Omega R_p C_p} = 4.314mV$, adopted from our previous work [32]. The dimensional RMS power can also be computed from

$$\tilde{P}_{rms} = \frac{\vartheta_0 V_{rms}^2}{R_L}, \quad (47)$$

where the value of load resistance is taken as $R_L = 10k\Omega$ for calculation purposes. Other parameters are $\alpha = 0.3, \beta = 0.03, \gamma = 0.1, \lambda = 0.2213, \mu_p = 0.12, N_1 = 0.98, \chi = 0.0002, \Lambda = 500000, \Theta = 0.0003, \rho = 1, \Omega = 2.095, v_b = 0.1, \mu_s = 0.9$, except where it is explicitly stated. Additionally, the following relations hold for $\bar{\mu}_1$ and $\bar{\mu}_3$;

$$\begin{cases} \bar{\mu}_1 = \frac{3}{2} \frac{\mu_s - \mu_m}{v_m}, \\ \bar{\mu}_3 = \frac{1}{2} \frac{\mu_s - \mu_m}{v_m^3}, \end{cases} \quad (48)$$

where $v_m = f(v_b)$ and $\mu_m = f(\mu_s)$.

4.1 Bifurcation analysis

One of the critical components affecting the behavioral stability of the system is the belt speed v_b .

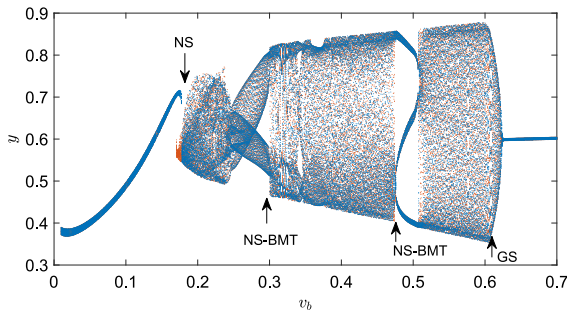


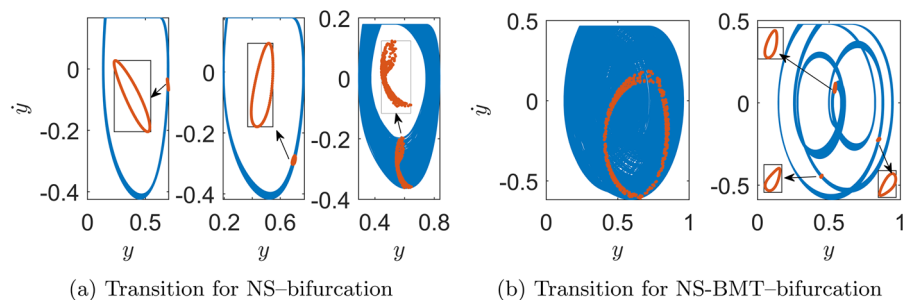
Fig. 8 Coexisting bifurcation diagram with v_b as the control parameter. The blue curve corresponds to forward sweep, while the red corresponds to backward sweep. (Color figure online)

It is responsible for injecting a variant form of energy into the structural dynamics as friction-induced self-excitation. Using this variable as the control parameter, a coexisting bifurcation diagram is constructed in Fig. 8. The blue curve is obtained during the forward sweep, while the red (underlaid) is obtained during the backward sweep, both on the hyperplane $x - y$. Three types of bifurcations are notable: the Neimark–Sacker (NS), Neimark–Sacker bifurcation to multiple tori (NS-BMT), and grazing–sliding (GS) bifurcation.

Figure 9a shows the transition for the NS bifurcation occurring at $v_b = [0.166, 0.177, 0.179]$ in which the limit cycle (inset) on the left-hand side (LHS) changes shape to one in the middle and is finally destroyed, giving birth to an entirely new attractor (inset) on the right-hand side (RHS). In Fig. 9b, the NS-BMT is one that gives birth to n-torus via NS bifurcation [37], and is demonstrated at $v_b = [0.466, 0.478]$ in which a single torus formed by the Poincaré section on the LHS bifurcates into 3-torus demonstrated by the inset of the attractor’s Poincaré on the RHS.

Finally, the GS bifurcation happens at $v_b = 0.607$ as shown in Fig. 11a (middle). At $v_b = 0.603$, the system is still characterized by stick-slip motion as seen on the LHS. But at grazing–sliding bifurcation (middle),

Fig. 9 Phase portraits with Poincaré sections showing the transition for the NS–bifurcation in (a) and NS-BMT in (b), both with reference to Fig. 8



the system’s speed \dot{y} grazes the touchline belt speed v_b before sliding back into motion. The attractor on the RHS shows clearly when the system is in pure slip motion as $\dot{y} < v_b$. The second principal influencer of the induced excitation is the coefficient of static friction μ_s . This is critical because, over time, the belt surface loses some roughness and affects the stick-slip motion of the mass. Fig. 10 shows the coexisting bifurcation diagram of the system, with μ_s as the control parameter. Discontinuity-induced bifurcation of torus (DIB-T) and NS-BMT are identified at $\mu_s \approx 0.6630$, and $\mu_s \approx 0.7431$, or $\mu_s \approx 0.8276$, respectively. The DIB-T [38] is examined in Fig. 11b, where the limit cycle in Fig. 11b (i) is destroyed via the transition in Fig. 11b (ii) to give birth to the torus of the Poincaré section in Fig. 11b (iii) as the system’s speed \dot{y} grazes the belt speed v_b held constant at $v_b = 0.45$. These dynamics have effects on energy harvesting, which are further investigated in the next subsection.

4.2 Effect of behavioral dynamics on energy

On the effects of qualitative changes occurring within the structural dynamics on energy harvesting, the bifurcation diagram of the system is constructed and plotted alongside the harvested energy to highlight the energy’s responses to certain types of bifurcation. The metric used for measuring energy harvesting is the root mean square voltage V_{rms} according to Eq. (46).

We begin by examining the system without coupling the electrical subcircuit of the van der Pol oscillator. In this case, only the simple mechanical substructure is present as a 1 DoF system, and the governing equations in Eq. (9) reduce to

$$\begin{cases} \ddot{y} + \beta\dot{y} + y + \gamma y^3 + \chi\phi - \rho\mu(\bar{v}_r) + \lambda y = 0, \\ \dot{\phi} + \Theta\phi - \chi\Lambda\dot{y} = 0. \end{cases} \tag{49}$$

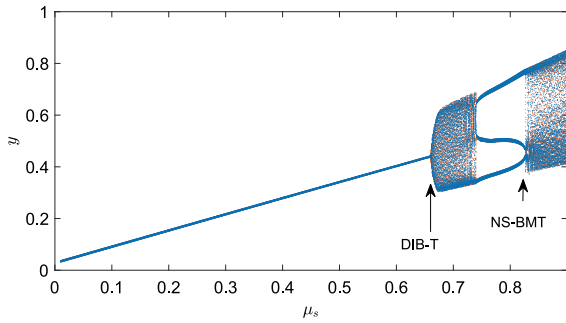


Fig. 10 Coexisting bifurcation diagram with μ_s as the control parameter. The blue curve corresponds to forward sweep, while the red corresponds to backward sweep. (Color figure online)

Using v_b as the control parameter, Fig. 12 is constructed, showing the bifurcation diagram in red (axis on the right) overlaid with the generated voltage in blue (axis on the left). It can be seen that the harvested energy (V_{rms}) is characteristically low (i.e., $V_{rms} < 1$) all through the system’s dynamics. The highest voltage is recorded at the GS bifurcation ($v_b \approx 0.6$) where $V_{rms} \approx 0.6$, after which the voltage falls to $V_{rms} = 0.53$ for $v_b \geq 0.64$. In comparison with the originally proposed design having the parametric coupling with the van der Pol oscillator whose dynamic model is given by Eq. (9), and using the same system parameters, Fig. 13a is constructed, with v_b as the bifurcation parameter. It can be seen that the energy harvested in this case is much higher (i.e., $V_{rms} > 100$ for all $v_b > 0.076$). Furthermore, this figure shows

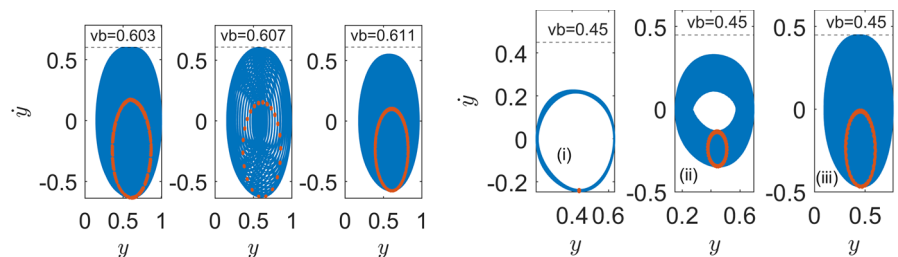
two kinds of bifurcation with significant changes in the level of harvested energy. First, the V_{rms} increases exponentially from near zero value until it reaches $V_{rms} = 207.4$ just before the NS bifurcation point ($v_b \approx 0.177$). At this point, V_{rms} jumps to a lower level ($V_{rms} \approx 156$) before increasing further at a slow pace. The steady increase, though small, terminates at NS–BMT, after which a fairly steady and stable energy is harvested. At GS bifurcation ($v_b \in [0.603, 0.611]$), another jump to a lower energy level ($V_{rms} \approx 149.7$) was recorded. After GS bifurcation, the system enters a pure slip motion, and this steady generated voltage level is maintained. Hence, the proposed model not only overcomes the limitation of low energy generation associated with the simple 1 DoF system but also generates higher (useful) energy over a wide range of belt speeds.

With μ_s as the bifurcation parameter, the harvested energy is fairly constant at $V_{rms} \approx 150$ until DIB-T as shown in Fig. 13b.

At DIB-T, there is a jump in harvested energy to a higher level. However, the new energy level is hard to maintain at a steady pace due to the underlying system’s dynamics for $\mu_s > 0.731$. At NS–BMT, a further jump in V_{rms} to a higher level is seen. However, the voltage is not smooth at this level but increases gradually for $\mu_s > 0.852$.

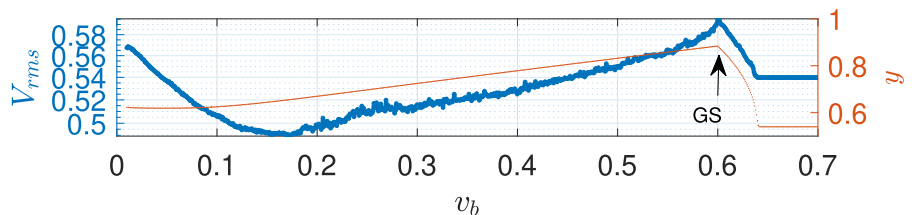
Examining the system’s dynamics and the energy harvested with respect to the variation of the internal parametric coupling strength μ_p , Fig. 14a is con-

Fig. 11 Phase portraits with Poincaré sections showing the transition for the GS–bifurcation in (a) and DIB-T in (b), with reference to Figs. 8 and 10, respectively



(a) Transition for the GS with reference to Fig. 8 (b) Transition for DIB-T at (i) $\mu_s = 0.6557$, (ii) $\mu_s = 0.6630$, and (iii) $\mu_s = 0.6719$, (in Fig. 10).

Fig. 12 Voltage generated (V_{rms}) in log scale (blue) and the bifurcation diagram (red), with v_b as the control parameter of the system without coupling. (Color figure online)



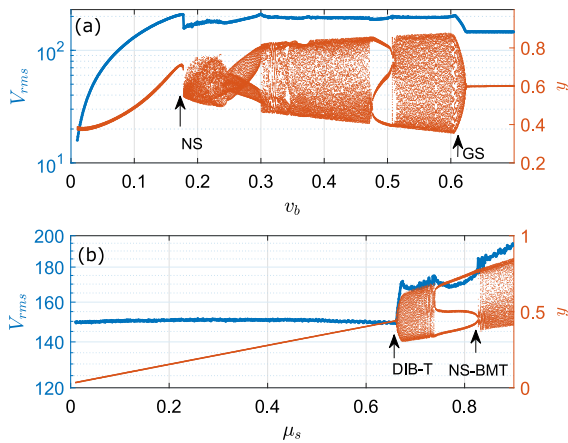


Fig. 13 Voltage generated (V_{rms}) in log scale (blue) and the bifurcation diagram (red), with v_b as the control parameter in **a**, and μ_s as the control parameter in **b**

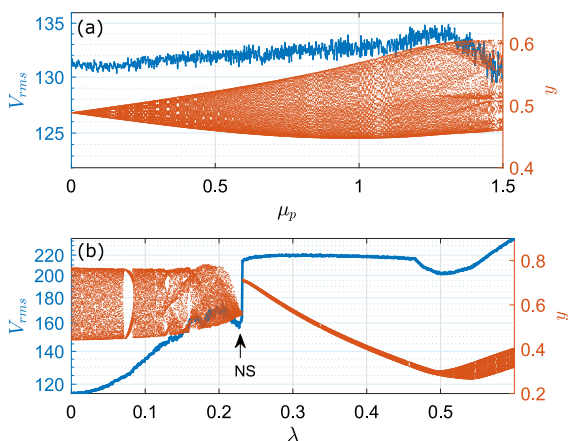


Fig. 14 Voltage generated (V_{rms}) in log scale (blue) and the bifurcation diagram (red), with μ_p as the control parameter in **a**, and λ as the control parameter in **b**. (Color figure online)

structured using μ_p as the control parameter. It can be seen from this figure that μ_p did not cause a distinctive bifurcation phenomenon, but one can identify the region of soft, intermediate, and hard coupling. In the soft coupling $\mu_p < 0.1$, the energy V_{rms} is mildly rough in the neighborhood of $V_{rms} \approx 131$. In the intermediate region $\mu_p \in [0.1, 1.12]$, the degree of roughness in $V_{rms} \approx 132.5$ increases. Hard coupling at $\mu_p \geq 1.12$ shows a decline in the energy harvested.

For the external coupling strength λ , the system experienced rich dynamics. Fig. 14b shows the constructed bifurcation diagram with λ as the control parameter. The energy V_{rms} increases steadily until it approaches the neighborhood of NS bifurcation ($\lambda \approx$

0.2231). At NS bifurcation point, V_{rms} jumps from about 160 to 220, and remains steady at this level until another behavioral change occurs at $\lambda \geq 0.4642$. Furthermore, a parametric study was conducted under the soft, intermediate, and hard internal parametric coupling to examine the harvested energy, and presented in Fig. 15.

Fixing the values of $\mu_p = 0.05$, $\mu_p = 0.12$, and $\mu_p = 1.12$, respectively for the soft, intermediate, and hard coupling, Fig. 15a shows the V_{rms} under these conditions with varying v_b . From this figure, the effect is slightly desirable under the soft and intermediate couplings. With μ_s as the varying parameter (Fig. 15b), the jumps to higher voltage levels under soft and intermediate couplings are desirable as they generate more energy. Finally, in the case of λ as the varying parameter (Fig. 15c), the generated voltages under these conditions are quantified as follows. For $\lambda < 0.2$, the highest energy is harvested at about $\tilde{V}_{rms} = 726.9$ mV corresponding to dimensional RMS power $\tilde{P}_{rms} = 12.25$ mW under soft and intermediate couplings. In the region $\lambda \in [0.2, 0.4]$, energy harvested under intermediate coupling is the highest, with $\tilde{P}_{rms} = 20.86$ mW. However, for $\lambda > 0.4$, the hard coupling produced the highest energy with $\tilde{P}_{rms} = 31.25$ mW.

5 Experimental setup

An experiment is performed to qualitatively verify the model in this section. The experimental stand in Fig. 16 is a multipurpose rig configured to accommodate the major features of the conceptual framework in Fig. 1 without the energy harvester. In Fig. 16, the air preparation module (valve with gauge and filter) labeled 1 uses the air at set pressure from the compressor and controls the aerostatic bearing 4, to give the body frame with masses 3 and 5 a frictionless swing on the attached handle. The body frame is attached to springs 6 on both sides.

The mass 3 is a rotor, providing unbalanced rotation on the body frame, and it is controlled by the first stepper motor driver 2, which takes input from computer 12 running the real-time electrical subcircuit simulation diagram in LabVIEW. The speed of the belt 7 is controlled by the second motor driver 10, which also takes input from the second signal generator 11.

A PC-based National Instrument Data Acquisition (NI DAQ) module 9 is connected to the computer

Fig. 15 Voltage generated (V_{rms}) at soft, intermediate, and hard internal parametric coupling (strength with μ_p), while varying v_b in (a), μ_s in (b), λ in (c)

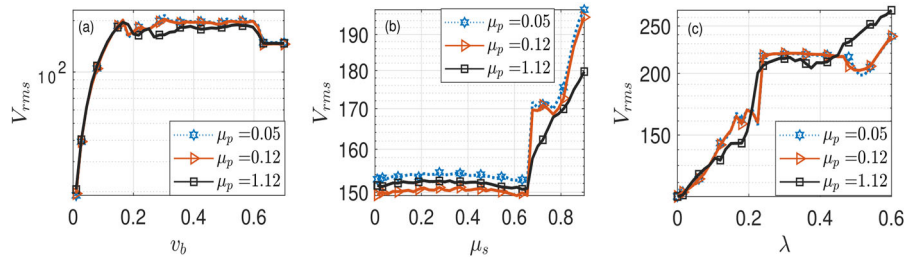
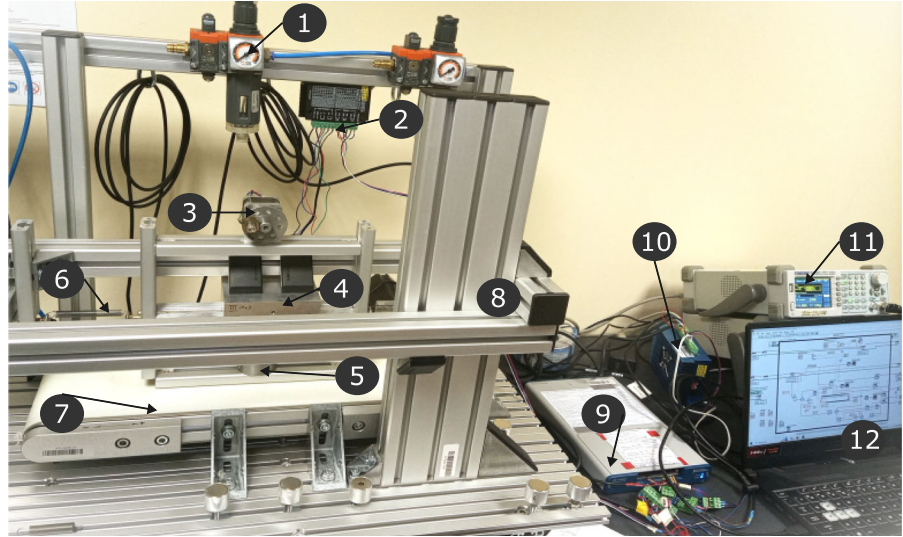


Fig. 16 Experimental setup with whole system (a) and enlarged portion (b).

1—valve, 2—motor driver, 3—unbalanced rotor, 4—aerostatic bearing, 5—body frame with mass, 6—spring, 7—belt support and drive, 8—support frame, 9—NI DAQ, 10—motor driver 2, 11—Signal generators (1 and 2), 12—computer with LabVIEW



system 12, with LabVIEW software to capture the dynamic responses which are saved to Excel spreadsheet. It should be noted that label 8 provides the support for the mechanical part while label 3 provides the unbalanced rotation that incorporates the parametric coupling. This setup is without the energy harvesting component, which reduces complexities in the implementation.

When valve 1 is turned ON, and the speed of the belt 7 is set, the speed of the unbalanced mass 3 is provided from the van der Pol electrical subcircuit drawn in LabVIEW running on the computer 12. The frame with the masses 3 and 5 as one lumped mass experiences displacement, and it is captured by the computer system 12 via module 9. This way, the setup is used to qualitatively compare the results of the numerical simulations with the experimental results after minor preprocessing to remove dead zones and timing alignments. Figure 17 shows the sampled current generated by the van der Pol electrical subcircuit in LabVIEW as the driving signal for the unbalanced rotor 3, and the corresponding pulse width modulation (PWM) voltage

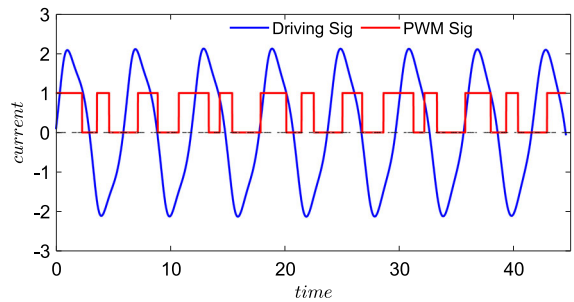


Fig. 17 Driving current from the van der Pol electrical subcircuit and associated PWM signal for driving the unbalanced rotor at slow-fast speed from the experiment

signal from the first signal generator. This ensures that the speed of the rotor is not constant but varies based on the current generated from the electrical subcircuit.

Figures 18, 19 and 20 compare the results of the numerical simulations (a) and the experimental verifications (b) of the system under three scenarios, in which the experimental results were scaled to their respective non-dimensional values using the relations estab-

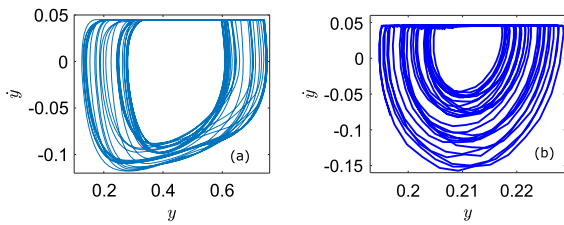


Fig. 18 Quasiperiodic phase portrait of numerical (a) $v = 0.045$, $\mu_s = 0.517$ and experimental (b) $v_0 = 0.007$ m/s; during stick-slip phenomenon

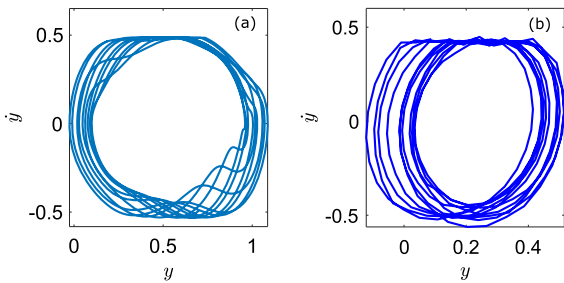


Fig. 19 Phase portrait of numerical **a** $v = 0.485$, $\mu_s = 0.65$ and experimental **b** $v_0 = 0.147$ m/s; near the grazing-sliding phenomenon

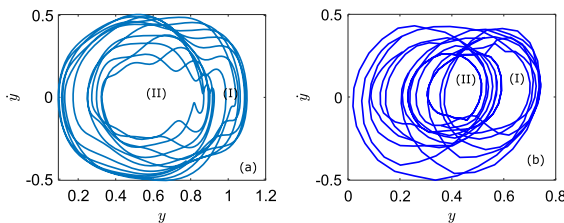


Fig. 20 Phase portrait of numerical **a** $v = 0.56$, $\mu_s = 0.85$ and experimental **b** $v_0 = 0.15$ m/s; during pure-slip motion

lished in Sect. 2.2. In Fig. 18, the system is entirely in the stick-slip quasiperiodic motion; the phase portraits show this phenomenon in both the numerical (a) and experimental (b) results when the belt's speed is kept at $v_0 = 0.007$ m/s. Increasing the belt's speed to $v_0 = 0.147$ m/s brought the system close to the grazing-sliding in Fig. 19. It should be noted that due to the high sensitivity of the system to the belt's speed and other assumptions and nonlinear effects present in the experimental setup, the exact grazing speed was hard to find. This is shown when the speed was increased to $v_0 = 0.15$ m/s, the system entered into pure-slip motion with two quasiperiodic orbits (I) and (II) respectively in Fig. 20 for both numerical (a) and experimental (b) results. All the parameter values are fixed as previ-

ously, except for those indicated in the figure captions. The experiment results verified the model qualitatively. However, some results are not the exact match due to the following assumptions and limitations:

- (i) The two linear springs estimate the nonlinear spring in the setup,
- (ii) The coefficient of static friction μ_s on the belt's surface reduces from the actual value due to long usage.

6 Concluding remarks

The governing equations for the dynamics of the parametrically coupled electromechanical structure were established. The system was solved analytically using the multiple scales method and validated by numerical simulation. The analytical treatment reveals the various parametric resonances captured in the frequency response of the system. The global dynamics of the structure were investigated, and nonlinear behaviors such as Neimark-Sacker (NS) bifurcation, NS-bifurcation to multiple tori, grazing-sliding bifurcation, and discontinuity-induced bifurcation of torus were identified. The effects of these qualitative changes on harvested energy were also investigated. At these bifurcation points, there are changes in the level of harvested energy in the form of jumps. At the NS bifurcation point, the harvested energy jumps to a higher level, while at grazing-sliding, it decreases to a lower level. The effects of parametric couplings were also examined. The greatest energy was harvested under the hard coupling with a quantified RMS power of 31.25 mW. The investigated model overcomes the limitations of low energy harvesting associated with the simple uncoupled system of the same kind. Finally, the experimental verification of the model was carried out to qualitatively validate the numerical methods.

Acknowledgements This work has been completed while the first author, Godwin Sani, was a Doctoral Candidate in the Interdisciplinary Doctoral School at the Lodz University of Technology, Poland

Funding This work has been supported by the Polish National Science Centre, Poland, under the grant OPUS 18 No. 2019/35/B/ST8/00980.

Data Availability Statement The study did not collect any data.

Declarations

Conflict of interest On behalf of all authors, the corresponding author states that there is no conflict of interest.

Open Access This article is licensed under a Creative Commons Attribution 4.0 International License, which permits use, sharing, adaptation, distribution and reproduction in any medium or format, as long as you give appropriate credit to the original author(s) and the source, provide a link to the Creative Commons licence, and indicate if changes were made. The images or other third party material in this article are included in the article's Creative Commons licence, unless indicated otherwise in a credit line to the material. If material is not included in the article's Creative Commons licence and your intended use is not permitted by statutory regulation or exceeds the permitted use, you will need to obtain permission directly from the copyright holder. To view a copy of this licence, visit <http://creativecommons.org/licenses/by/4.0/>.

References

- Garud, M., Pratap, R.: Mems audio speakers. *J. Micromech. Microeng.* **34**(1), 013001 (2023). <https://doi.org/10.1088/1361-6439/acfe86>
- Koudafokè, G.N., Hinvì, L.A., Miwadinou, C.H., Monwanou, A.V., Orou, J.B.C.: Passive sensor with Josephson junction coupled to an electric resonator and a nanobeam. *Sensors Actuators A Phys.* **318**, 112509 (2021). <https://doi.org/10.1016/j.sna.2020.112509>
- Hu, Y., Bu, S., Yi, S., Zhu, J., Luo, J., Wei, Y.: A novel energy flow analysis and its connection with modal analysis for investigating electromechanical oscillations in multi-machine power systems. *IEEE Trans. Power Syst.* **37**(2), 1139–1150 (2022). <https://doi.org/10.1109/TPWRS.2021.3099474>
- Xu, X., Ju, W., Wang, B., Sun, K.: Real-time damping estimation on nonlinear electromechanical oscillation. *IEEE Trans. Power Syst.* **36**(4), 3142–3152 (2021). <https://doi.org/10.1109/TPWRS.2020.3042096>
- Kenmogne, F., Wokwenmendiam, M.L., Simo, H., Adile, A.D., Noah, P.M.A., Barka, M., Nguïya, S.: Effects of damping on the dynamics of an electromechanical system consisting of mechanical network of discontinuous coupled system oscillators with irrational nonlinearities: Application to sand sieves. *Chaos Solitons Fractals* **156**, 111805 (2022). <https://doi.org/10.1016/j.chaos.2022.111805>
- Ramadoss, J., Kengne, J., Tanekou, S.T., Rajagopal, K., Kenmoe, G.D.: Reversal of period doubling, multistability and symmetry breaking aspects for a system composed of a van der Pol oscillator coupled to a Duffing oscillator. *Chaos Solitons Fractals* **159**, 112157 (2022). <https://doi.org/10.1016/j.chaos.2022.112157>
- Balamurali, R., Kengne, J., Goune Chengui, R., Rajagopal, K.: Coupled van der Pol and Duffing oscillators: emergence of antimonotonicity and coexisting multiple self-excited and hidden oscillations. *Eur. Phys. J. Plus* **137**(7), 789 (2022). <https://doi.org/10.1140/epjp/s13360-022-03000-2>
- Lyu, W., Li, S., Huang, J., Bi, Q.: Occurrence of mixed-mode oscillations in a system consisting of a van der pol system and a duffing oscillator with two potential wells. *Nonlinear Dyn.* (2024). <https://doi.org/10.1007/s11071-024-09322-3>
- Sani, G., Awrejcewicz, J., Tabekoueng, Z.N.: Modeling, analysis and control of parametrically coupled electromechanical oscillators. *Mech. Mach. Theory* **191**, 105514 (2024). <https://doi.org/10.1016/j.mechmachtheory.2023.105514>
- Pedro, B.G., Bertemes-Filho, P.: A new impedance sensor based on electronically implemented chaotic coupled van der pol and damped duffing oscillators. *Front. Electron.* **3**, 797525 (2022). <https://doi.org/10.3389/felec.2022.797525>
- Balaram, B., Santhosh, B., Awrejcewicz, J.: Frequency entrainment and suppression of stick-slip vibrations in a 3 dof discontinuous disc brake model. *J. Sound Vib.* **538**, 117224 (2022). <https://doi.org/10.1016/j.jsv.2022.117224>
- Sulollari, E., van Dalen, K.N., Cabbai, A.: Vibration-induced friction modulation for a general frequency of excitation. *J. Sound Vib.* **573**, 118200 (2024). <https://doi.org/10.1016/j.jsv.2023.118200>
- Wang, X.C., Huang, B., Wang, R.L., Mo, J.L., Ouyang, H.: Friction-induced stick-slip vibration and its experimental validation. *Mech. Syst. Signal Process.* **142**, 106705 (2020). <https://doi.org/10.1016/j.ymsp.2020.106705>
- Peng, Y., Fan, J.: Discontinuous dynamics of a class of 3-dof friction impact oscillatory systems with rigid frame and moving jaws. *Mech. Mach. Theory* **175**, 104931 (2022). <https://doi.org/10.1016/j.mechmachtheory.2022.104931>
- Sani, G., Balaram, B., Awrejcewicz, J.: Nonlinear interaction of parametric excitation and self-excited vibration in a 4 dof discontinuous system. *Nonlinear Dyn.* **111**(3), 2203–2227 (2023). <https://doi.org/10.1007/s11071-022-07931-4>
- Li, Z., Ouyang, H., Wei, Z.-H.: Insights into instability of friction-induced vibration of multi-degree-of-freedom models. *J. Sound Vib.* **503**, 116107 (2021). <https://doi.org/10.1016/j.jsv.2021.116107>
- Hu, H., Batou, A., Ouyang, H., Liu, N.: Friction-induced planar vibration of a two-rigid-disc system with a finite contact area subjected to uncertain friction. *Nonlinear Dyn.* **111**, 18677–18696 (2023). <https://doi.org/10.1007/s11071-023-08851-7>
- Kumar, G., Malas, A.: Control of friction induced oscillation by displacement feedback with a second order filter. *J. Sound Vib.* (2024). <https://doi.org/10.1016/j.jsv.2024.118345>
- Dou, C., Fan, J., Li, C., Cao, J., Gao, M.: On discontinuous dynamics of a class of friction-influenced oscillators with nonlinear damping under bilateral rigid constraints. *Mech. Mach. Theory* **147**, 103750 (2020). <https://doi.org/10.1016/j.mechmachtheory.2019.103750>
- Liu, N., Ouyang, H.: Friction-induced vibration considering multiple types of nonlinearities. *Nonlinear Dyn.* **102**, 2057–2075 (2020). <https://doi.org/10.1007/s11071-020-06055-x>
- Zhang, R., Zhang, H., Zanonì, A., Wang, Q., Masarati, P.: A tight coupling scheme for smooth/non-smooth multi-body co-simulation of a particle damper. *Mech. Mach. Theory* **161**, 104181 (2021). <https://doi.org/10.1016/j.mechmachtheory.2020.104181>
- Iqbal, M., Nauman, M.M., Khan, F.U., Abas, P.E., Cheok, Q., Iqbal, A., Aissa, B.: Vibration-based piezoelectric, electromagnetic, and hybrid energy harvesters for microsystems applications: A contributed review. *Int. J. Energy Res.* **45**(1), 65–102 (2021). <https://doi.org/10.1002/er.5643>

23. Kang, X., Tang, J., Xia, G., Wei, J., Zhang, F., Sheng, Z., et al.: Design, optimization, and application of nonlinear energy sink in energy harvesting device. *Int. J. Energy Res.* (2024). <https://doi.org/10.1155/2024/2811428>
24. Di Persio, F., Blecua, M., Chaine, A.C., Daue, T., Mateo-Mateo, C., Ezpeleta, I., Pötschke, P., Krause, B., Inci, E., Pionteck, J., et al.: Recyclability of novel energy harvesting and storage technologies for IoT and wireless sensor networks. *J. Clean. Prod.* (2024). <https://doi.org/10.1016/j.jclepro.2023.140525>
25. Sun, Y., Li, Y.-Z., Yuan, M.: Requirements, challenges, and novel ideas for wearables on power supply and energy harvesting. *Nano Energy* **115**, 108715 (2023). <https://doi.org/10.1016/j.nanoen.2023.108715>
26. Cao, H., Kong, L., Tang, M., Zhang, Z., Wu, X., Lu, L., Li, D.: An electromagnetic energy harvester for applications in a high-speed rail pavement system. *Int. J. Mech. Sci.* **243**, 108018 (2023). <https://doi.org/10.1016/j.ijmecsci.2022.108018>
27. Wang, D.W., Liu, M.X., Qian, W.J., Wu, X., Ma, Q., Wu, Z.Q.: Parametrical investigation of piezoelectric energy harvesting via friction-induced vibration. *Shock Vib.* (2020). <https://doi.org/10.1155/2020/6190215>
28. Han, Y., Zhang, Z.: Nonlinear energy harvesting system with multiple stability. <https://doi.org/10.48550/arXiv.2312.17282> arXiv preprint arXiv:2312.17282 (2023)
29. Xiang, Z.Y., Mo, J.L., Qian, H.H., Chen, W., Luo, D.B., Zhou, Z.R.: Friction-induced vibration energy harvesting of a high-speed train brake system via a piezoelectric cantilever beam. *Tribol. Int.* **162**, 107126 (2021). <https://doi.org/10.1016/j.triboint.2021.107126>
30. Xiao, Y., Karnaoukh, S., Wu, N.: Design and analysis of a d15 mode piezoelectric energy generator using friction-induced vibration. *Smart Mater. Struct.* **32**(3), 035040 (2023). <https://doi.org/10.1088/1361-665X/acbcb1>
31. Chen, W., Mo, J., Ouyang, H., Xiang, Z., Zhao, J.: A bistable energy harvester for friction-induced stick-slip vibration. *Nonlinear Dyn.* (2023). <https://doi.org/10.1007/s11071-023-09055-9>
32. Sani, G., Balam, B., Kudra, G., Awrejcewicz, J.: Energy harvesting from friction-induced vibrations in vehicle braking systems in the presence of rotary unbalances. *Energy* **289**, 130007 (2024). <https://doi.org/10.1016/j.energy.2023.130007>
33. Iqteit, N.A., Yahya, K., Makahleh, F.M., Attar, H., Amer, A., Solyman, A.A.A., Qudaimat, A., Tamizi, K.: Simple mathematical and simulink model of stepper motor. *Energies* **15**(17), 6159 (2022). <https://doi.org/10.3390/en15176159>
34. Filippov, A.F.: *Differential Equations with Discontinuous Righthand Sides: Control Systems*. Springer, New York (2013). <https://doi.org/10.1007/978-94-015-7793-9>
35. Awrejcewicz, J., Starosta, R., Sypniewska-Kamińska, G.: *Asymptotic Multiple Scale Method in Time Domain: Multi-Degree-of-Freedom Stationary and Nonstationary Dynamics*. CRC Press, Boca Raton (2022)
36. Das, K., Kumar, R., Krishna, A.: Analyzing electric vehicle battery health performance using supervised machine learning. *Renew. Sustain. Energy Rev.* **189**, 113967 (2024). <https://doi.org/10.1016/j.rser.2023.113967>
37. Stankevich, N.: Stabilization and complex dynamics initiated by pulsed force in the rössler system near saddle-node bifurcation. *Nonlinear Dyn.* **112**, 2949–2967 (2024). <https://doi.org/10.1007/s11071-023-09183-2>
38. Bernardo, M., Hogan, S.J.: Discontinuity-induced bifurcations of piecewise smooth dynamical systems. *Philos. Trans. R. Soc. A Math. Phys. Eng. Sci.* **368**(1930), 4915–4935 (2010). <https://doi.org/10.1098/rsta.2010.0198>

Publisher's Note Springer Nature remains neutral with regard to jurisdictional claims in published maps and institutional affiliations.